



1        A derecho climatology (2004-2021) in the United States  
2        based on machine learning identification of bow echoes

3        Jianfeng Li<sup>1,\*</sup>, Andrew Geiss<sup>1</sup>, Zhe Feng<sup>1,\*</sup>, L. Ruby Leung<sup>1</sup>, Yun Qian<sup>1</sup>, Wenjun Cui<sup>2,3</sup>

4  
5        <sup>1</sup>Atmospheric, Climate, and Earth Sciences Division, Pacific Northwest National Laboratory,  
6        Richland, Washington, USA

7        <sup>2</sup>Cooperative Institute for Severe and High-Impact Weather Research and Operations, University  
8        of Oklahoma, Norman, Oklahoma, USA

9        <sup>3</sup>National Severe Storms Laboratory, National Oceanic and Atmospheric Administration,  
10        Norman, Oklahoma, USA

11        \*Correspondence to Jianfeng Li ([jianfeng.li@pnnl.gov](mailto:jianfeng.li@pnnl.gov)) and Zhe Feng ([zhe.feng@pnnl.gov](mailto:zhe.feng@pnnl.gov))

12



## 13 Abstract

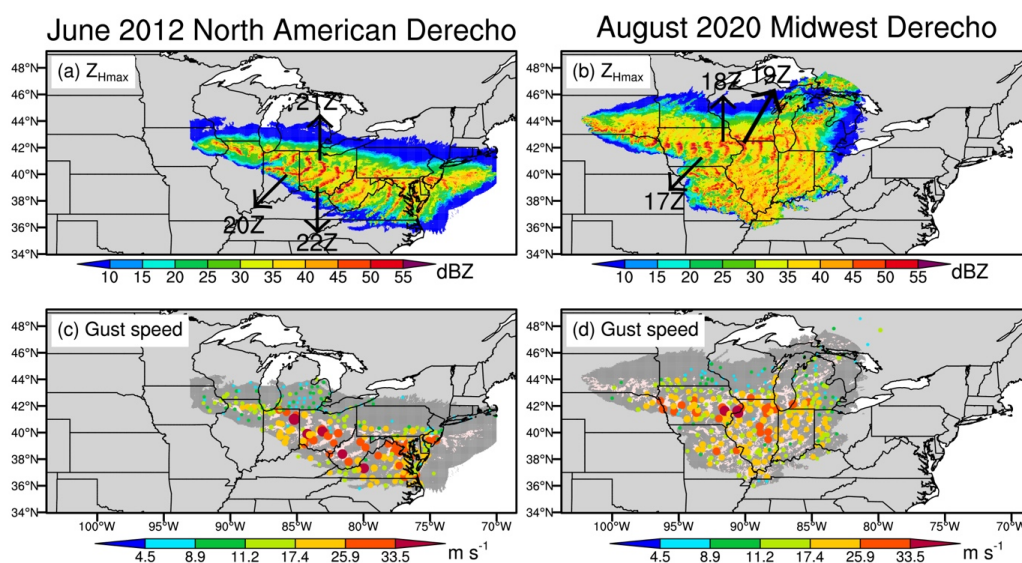
14 Due to their persistent widespread severe winds, derechos pose significant threats to human safety  
15 and property, and they are as hazardous and fatal as many tornadoes and hurricanes. Yet, automated  
16 detection of derechos remains challenging due to the absence of spatiotemporally continuous observations  
17 and the complex criteria employed to define the phenomenon. This study proposes a physically based  
18 definition of derechos that contains the key features of derechos described in the literature and allows  
19 their automated objective identification using either observations or model simulations. The automated  
20 detection is composed of three algorithms: the Flexible Object Tracker algorithm to track mesoscale  
21 convective systems (MCSs), a semantic segmentation convolutional neural network to identify bow  
22 echoes, and a comprehensive algorithm to classify MCSs as derechos or non-derecho events. Using the  
23 new approach, we develop a novel high-resolution (4 km and hourly) observational dataset of derechos  
24 over the United States east of the Rocky Mountains from 2004 to 2021. The dataset is analyzed to  
25 document the derecho climatology in the United States. Many more derechos (increased by ~50-400%)  
26 are identified in the dataset (~31 events per year) than in previous estimations (~6-21 events per year), but  
27 the spatial distribution and seasonal variation patterns resemble earlier studies with a peak occurrence in  
28 the Great Plains and Midwest during the warm season. In addition, around 20% of damaging gust ( $\geq$   
29  $25.93 \text{ m s}^{-1}$ ) reports are produced by derechos during the dataset period over the United States east of the  
30 Rocky Mountains. The dataset is available at <https://doi.org/10.5281/zenodo.10884046> (Li et al., 2024).

31



## 32 1 Introduction

33 A derecho is qualitatively defined as a widespread, long-lived straight-line windstorm associated  
34 with a fast-moving mesoscale convective system (MCS). Figure 1 shows two of the most destructive  
35 derechos in the United States: the June 2012 North American derecho and the August 2020 Midwest  
36 Derecho. Both events lasted for over 10 hours, with apparent bow echoes and extensive damaging wind  
37 gusts ( $\geq 25.93 \text{ m s}^{-1}$ ). Due to the persistent widespread damaging gusts, derechos can severely damage  
38 property and threaten human lives, as exemplified by the extensive power outages and more than ten  
39 fatalities caused by the two derechos. Ashley and Mote (2005) demonstrated that derechos could be as  
40 hazardous as and were comparable in magnitude to most hurricanes and tornadoes in the United States  
41 between 1986 and 2003.



42  
43 Figure 1. Spatial evolutions of the (a, b) composite (column-maximum) radar reflectivity ( $Z_{Hmax}$ ) signatures  
44 and (c, d) surface gust speeds (colored dots) of two derechos. The first column is for the June 2012 North  
45 American derecho, which occurred on 29-30 June 2012, and the right column is for the August 2020 Midwest  
46 derecho, which occurred on 10-11 August 2020. Due to spatiotemporal overlapping, multiple  $Z_{Hmax}$  and gust  
47 speeds may exist for a given grid cell or weather station, in which case only the corresponding maximums are  
48 shown in the figure. The timings of some bow echo occurrences are labeled in (a) and (b). In (a), “20Z”,  
49 “21Z”, and “22Z” refer to 20:00, 21:00, and 22:00 UTC on 29 June 2012. In (b), “17Z”, “18Z”, and “19Z”  
50 refer to 17:00, 18:00, and 19:00 UTC on 10 August 2020. In (c) and (d), the misty rose shading corresponds to  
51 areas with  $Z_{Hmax} \geq 40 \text{ dBZ}$ , and the dark gray shading refers to derecho coverage with  $Z_{Hmax} < 40 \text{ dBZ}$ . The dot



52 sizes in (c) and (d) are proportional to the gust speed magnitudes. Notably, gust speed in (c) and (d) is based on  
53 the hourly maximum gust speed ( $gust_{hourly\_max}$ ), which is the largest gust speed within one hour if multiple gust  
54 speed measurements are available.

55 A reliable derecho dataset is foundational for understanding the underlying physical mechanism of  
56 derecho initiation and development and their socioeconomic impacts. Johns and Hirt (1987) developed  
57 the first derecho climatology in the warm seasons of 1980-1983 in the United States by quantitatively  
58 defining a derecho as a family of downburst clusters produced by an extratropical MCS. Specifically, they  
59 required a derecho to satisfy the following six criteria. 1) There must be a concentrated area of reports  
60 with wind damage or convective gusts  $> 25.7 \text{ m s}^{-1}$ , with a major axis length of at least 400 km. 2) These  
61 reports must show a pattern of chronological progression, either as a singular swath or a series of swaths.  
62 3) The concentrated area must have at least three reports of either F1 damage ( $32.7\text{-}50.3 \text{ m s}^{-1}$ ) (Fujita,  
63 1971) or convective gust of at least  $33.4 \text{ m s}^{-1}$  separated by  $\geq 64 \text{ km}$ . 4) At most 3 hours can elapse  
64 between successive reports of wind damage or gust  $> 25.7 \text{ m s}^{-1}$ . 5) The associated convective system  
65 must have temporal and spatial continuity in surface pressure and wind fields. 6) If multiple swaths of  
66 wind damage or gust reports  $> 25.7 \text{ m s}^{-1}$  exist, they must be from the same MCS event. Since then,  
67 several other studies have developed derecho climatologies during other periods using slightly different  
68 criteria (Bentley and Mote, 1998; Evans and Doswell, 2001; Bentley and Sparks, 2003; Coniglio and  
69 Stensrud, 2004; Guastini and Bosart, 2016). For example, Bentley and Mote (1998) removed the third  
70 requirement and reduced the elapsed time in the fourth condition from no more than 3 hours to no more  
71 than 2 hours in their derecho climatology from 1986 to 1996. In Coniglio and Stensrud (2004), the  
72 elapsed time was further changed to no more than 2.5 hours, and the gust reports of at least  $33 \text{ m s}^{-1}$  were  
73 used to separate derechos of different intensities.

74 Although the aforementioned derecho datasets were generated using different criteria and during  
75 different periods (Johns and Hirt, 1987; Bentley and Mote, 1998; Evans and Doswell, 2001; Bentley and  
76 Sparks, 2003; Coniglio and Stensrud, 2004; Guastini and Bosart, 2016), they showed many similar  
77 derecho climatological characteristics in the United States. For example, derechos occur more frequently



78 in the warm than cold seasons; the Great Plains, Midwest, and Ohio Valley are regions most favorable for  
79 derecho development, and few derechos occur in the eastern and western coastal areas. Considering the  
80 inconsistent thresholds used in the above studies and the lack of physical mechanisms in their derecho  
81 definitions, Corfidi et al. (2016) proposed a stricter and more physically based derecho definition, which  
82 required the existence of sustained bow echoes with mesoscale vortices or rear-inflow jets and a nearly  
83 continuous wind damage swath of at least 100 km wide along most of its extent and 650 km long. In  
84 addition, the wind damage must occur after the convective system was organized into a cold-pool-driven  
85 forward-propagating MCS. Most derechos satisfying this definition would be classified as “progressive”  
86 but not “serial.” A serial derecho typically originates in strongly forced environments and develops from a  
87 mature squall line with multiple embedded bow echoes. In contrast, progressive derechos generally  
88 originate from small convective clusters that grow upscale into large organized forward-propagating  
89 MCSs in synoptic environments with weak forcing (Squitieri et al., 2023).

90 It is difficult to develop a derecho climatology using the definition proposed by Corfidi et al. (2016)  
91 with current operational measurements, as it involves the identification of bow echoes, rear-inflow jets,  
92 and cold pools. However, rear-inflow jets and cold pools are generally associated with bow echoes  
93 (Weisman, 1993; Adams-Selin and Johnson, 2010). Once long-lived bow echoes are found in an MCS  
94 event, we can expect the simultaneous existence of rear-inflow jets and cold pools. Nevertheless,  
95 identifying bow echoes, a feature typically identified from radar observations, is still challenging for large  
96 volumes of data, such as the 30+ year National Oceanic and Atmospheric Administration (NOAA) Next  
97 Generation Weather Radar (NEXRAD) archive. The manual examination is time-consuming and sensitive  
98 to subjective biases. This study applies a semantic segmentation convolutional neural network (CNN) to  
99 detect bow echoes automatically from two-dimensional composite (column-maximum) reflectivity ( $Z_{Hmax}$ )  
100 data in the United States, which are then combined with an MCS tracking dataset and gust speed  
101 measurements from surface meteorological stations to identify derechos using criteria adjusted from  
102 Corfidi et al. (2016). After manual examination and validation, we produce a high-resolution (4 km and



103 hourly) observational derecho dataset in the United States east of the Rocky Mountains from 2004 to  
104 2021. As the first derecho climatology that utilizes a machine learning technique following physically  
105 based criteria and covers the recent decades, the dataset provides a reference for future derecho studies  
106 and can be used to investigate the underlying mechanisms for derecho initiation and development, the  
107 climatological impacts of derechos on hazardous weather, and the damage of derechos to infrastructure  
108 and human property.

109 The remainder of the paper is organized as follows. Section 2 introduces the MCS dataset and gust  
110 speed measurements used to generate the derecho dataset. Section 3 describes the machine learning (i.e.,  
111 semantic segmentation CNN) methodology to detect bow echoes, including sampling, training, and  
112 evaluation. Section 4 explains our derecho identification criteria in detail. Section 5 evaluates our derecho  
113 dataset against the observational data from the NOAA Storm Prediction Center (SPC) in 2004 and 2005.  
114 Section 6 analyzes the derecho climatological characteristics. Section 7 shows how to access our derecho  
115 dataset, and the study is summarized in Section 8.

## 116 **2 Source datasets**

### 117 **2.1 MCS dataset**

118 Since previous MCS datasets only cover the period from 2004 to 2017 (Li et al., 2021; Feng et al.,  
119 2019), we use an updated version of the Python FLEXible Object TRAcKeR (PyFLEXTRKR) software  
120 (Feng et al., 2023), which exploits collocated radar signatures, brightness temperature, and precipitation  
121 to identify robust MCS events (Feng et al., 2019), to produce an updated MCS dataset in the United States  
122 east of the Rocky Mountains from 2004 to 2021. Several source datasets are used in the generation of the  
123 MCS dataset, including the National Centers for Environmental Prediction (NCEP)/the Climate  
124 Prediction Center (CPP) L3 4 km Global Merged IR V1 brightness temperature dataset (Janowiak et al.,  
125 2017), the three-dimensional Gridded NEXRAD Radar (GridRad) dataset (Bowman and Homeyer, 2017),



126 the NCEP Stage IV precipitation dataset (CDIACS/EOL/NCAR/UCAR and CPC/NCEP/NWS/NOAA,  
127 2000), and hourly melting level heights derived from ERA5 (European Centre for Medium-Range  
128 Weather Forecasts (ECMWF) Reanalysis v5) (Hersbach et al., 2023). The MCS definition criteria are  
129 almost the same as those in Feng et al. (2019), such as cold cloud shield (CCS) area  $> 60,000 \text{ km}^2$ ,  
130 precipitation feature (PF, which is a continuous convective or stratiform area with surface rain rate  $> 2$   
131  $\text{mm h}^{-1}$ ) major axis length  $> 100 \text{ km}$ , the existence of 45-dBZ convective echoes, etc., except that the  
132 duration requirement is lowered to include those convective systems lasting for just 6 hours. This  
133 adjustment allows us to capture slightly shorter-lived MCSs that produce intense wind gusts but are  
134 missed in the previous MCS datasets. Convective and stratiform radar echo classification in  
135 PyFLEXTRKR follows the Storm Labeling in 3D (SL3D) algorithm (Starzec et al., 2017), which uses  
136 horizontal texture and vertical structure of radar reflectivity from the GridRad product. Notably, the  
137 GridRad data are available each month from 2004 to 2017 but only between April and August from 2018  
138 to 2021. Since most derechos occur in the warm season (Ashley and Mote, 2005; Coniglio and Stensrud,  
139 2004), missing the cold months between 2018 and 2021 does not affect our derecho climatological  
140 analyses in Section 6. For brevity, we do not mention the missing cold months between 2018 and 2021 in  
141 the following sections unless stated otherwise.

## 142 **2.2 Surface gust speed observations**

143 Surface gust speed measurements between 2004 and 2021 are from the Integrated Surface Database  
144 (ISD) (NOAA/NCEI, 2001), developed by the NOAA National Centers for Environmental Information  
145 (NCEI) in collaboration with several other institutions. ISD compiles global hourly and synoptic surface  
146 observations from numerous sources (e.g., the Automated Surface Observing System and the Automated  
147 Weather Observing System) into a single common format and data model. Besides internal quality control  
148 procedures conducted by the source datasets, ISD applies additional quality control algorithms to process  
149 each observation through a series of validity checks, extreme value checks, and internal and external



150 continuity checks (Smith et al., 2011). This study uses measurements passing all quality control checks  
151 (NOAA/NCEI, 2018). Notably, there may be multiple measurements at different times within one hour  
152 for some stations. To keep the sampling consistency across different datasets used in the derecho  
153 identification, we calculate  $gust_{hourly\_max}$ , which is the largest gust speed of all available measurements  
154 within one hour, for each observational site, unless stated otherwise. A total of 4,260 observational sites  
155 provide gust speed measurements between 2004 and 2021 in the study domain, of which 3,954 are over  
156 land, and the rest are over the ocean or lakes (Figure S1). We have excluded one observational site (ISD  
157 station ID: 726130-14755) in the northeastern United States, which has an unrealistic number of  
158 damaging gust measurements (more than 1,000 hours), inconsistent with the surrounding sites. We note  
159 that although we only use measurements passing all the available quality control checks, spatial quality  
160 control is missing in the ISD (Smith et al., 2011). Figure S2a shows that some sites in the eastern United  
161 States have apparently more damaging gust occurrences than their surrounding sites, but the occurrence  
162 frequencies are less than those stations around the Rocky Mountains. We do not have enough evidence to  
163 exclude them from the study. However, the quality of the gust speed measurements will undoubtedly be a  
164 source of uncertainty for our derecho dataset. In addition, only 420 sites have continuous gust  
165 measurements from 2004 to 2021, while the rest have gust measurements only during part of the study  
166 period. The availability of observational sites is another source of uncertainty when identifying derechos.

### 167 **3 Machine learning identification of bow echoes**

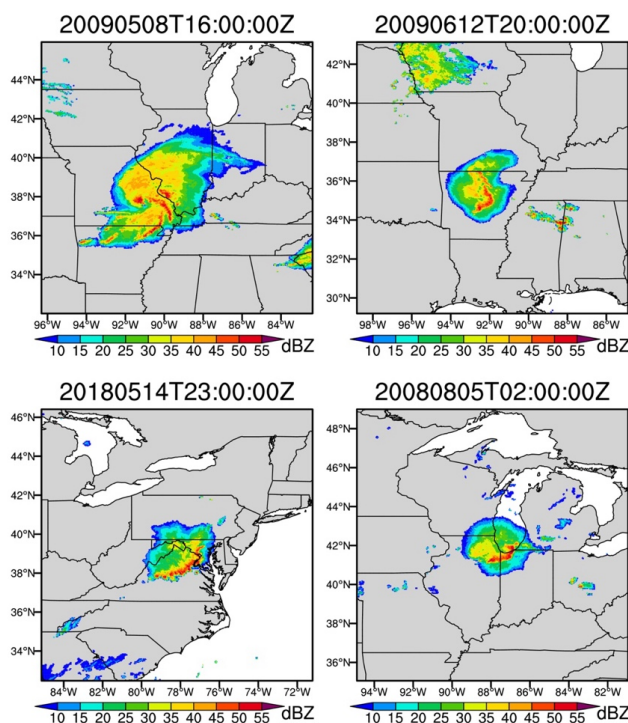
168 A bow echo is a bow-shaped pattern on a radar image, but its vague definition makes it hard to  
169 identify them extensively and efficiently using traditional methods. Instead, we train a semantic  
170 segmentation CNN to identify bow echoes automatically from two-dimensional  $Z_{Hmax}$  images by  
171 performing pixel-level labeling of the bow echo extent. Compared to the manual examination of radar  
172 images, machine learning can save a tremendous amount of time and eliminate subjective bias.



## 173 3.1 Bow Echo Samples

### 174 3.1.1 Initial manual sampling

175 Our initial bow echo samples are generated based on the named derechos on Wikipedia  
176 ([https://en.wikipedia.org/wiki/List\\_of\\_derecho\\_events](https://en.wikipedia.org/wiki/List_of_derecho_events); last access: 19 March 2023). We identify 54  
177 named derechos in the MCS dataset and manually label times with apparent bow echoes through visual  
178 inspection of  $Z_{Hmax}$  associated with the tracked MCSs. Each positive sample is a  $384 \times 384$ -pixel ( $\sim 1536$   
179  $\text{km} \times 1536 \text{ km}$ )  $Z_{Hmax}$  image centered at the corresponding derecho with a bow echo embedded (Figure 2).  
180 The number of bow echo samples varies among different derechos, and 566 positive samples are obtained  
181 in total. 5400 negative samples are also randomly selected from the radar reflectivity dataset.



182 Figure 2. Four examples of bow echoes from the named derechos. The color shading is for  $Z_{Hmax}$ . The subplot  
183 titles indicate the bow echo timings. For example, 20130613T04:00:00Z represents 4:00 UTC on 13 June  
184 2013.  
185



186 *3.1.2 CNN-based selection of additional bow echo samples*

187 Our initial attempt at developing an automated bow echo detection scheme is to train a classifier  
188 CNN — “Dense Net” (Huang et al., 2019) that ingests  $384 \times 384$ -pixel single-channel  $Z_{Hmax}$  images and  
189 outputs a single classification indicating the presence of a bow echo. Dense Nets are notable for their  
190 large number of skip connections, and they can achieve comparable performance to very large classifier  
191 CNNs with only a fraction of the trainable parameters. Unfortunately, a Dense Net trained on the  
192 aforementioned initial samples has a very high false positive rate when applied to the full radar dataset  
193 (determined by manual inspection). Although this Dense Net is unsuitable for deployment, the collection  
194 of new positive samples it successfully identifies allows us to supplement the list of known bow echoes  
195 and develop a more diverse training set for the following segmentation model.

196 *3.1.3 Pseudo-labeling*

197 By combining the initial samples and the manually selected true positives from the low-quality  
198 Dense Net model, we build a semantic segmentation training dataset of 500 unique bow echo snapshots  
199 and corresponding hand-drawn bow echo masks. While 500 positive samples are relatively small for a  
200 deep learning application, these samples have higher diversity than the initial bow echoes generated from  
201 the named derechos on Wikipedia because they are drawn from more distinct events, and, in general,  
202 semantic segmentation CNNs can be successfully trained with far fewer samples than image classification  
203 CNNs (Bardis et al., 2020).

204 A relatively low-skill version of the semantic segmentation CNN is trained using the 500 hand-  
205 labeled radar images and then applied to the entire  $Z_{Hmax}$  dataset. We manually review the bow echo  
206 masks produced by this segmentation model and add some of the high-quality masks to a new training  
207 dataset. We also collect some of its false positive masks as new negative samples in the new training  
208 dataset. This is a semi-supervised learning approach known as “pseudo-labeling” or “bootstrapping” (Van



209 Engelen and Hoos, 2020; Ouali et al., 2020) and is commonly applied to semantic segmentation problems  
210 because of the high expense of hand-drawn labels (Pelález-Vegas et al., 2023). The pseudo-labels and  
211 hand-labels are combined into a final training dataset with 3677 samples, including 1699 bow echoes and  
212 1978 negative samples, which is used to train the much more skillful semantic segmentation model in  
213 Section 3.2.

#### 214 *3.1.4 Data augmentation*

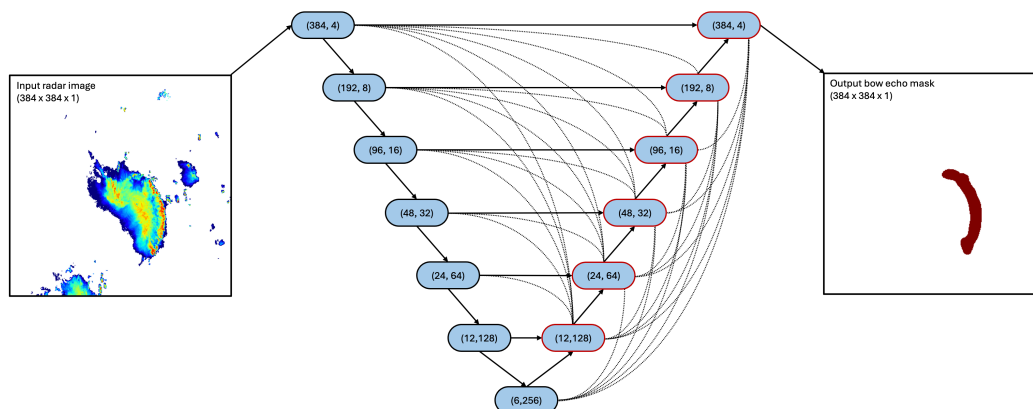
215 To combat the limited training data further, we use several data augmentation strategies when  
216 constructing training batches. During training, positive and negative samples are selected with equal  
217 probability, and a batch size of 8 is used. First, random salt and pepper noise is added to 10% of the pixels  
218 in each sample with a probability of 0.1. Second, weak random Gaussian noise with a standard deviation  
219 of 5 dBZ is added to all the pixels in each sample with a probability of 0.1. Third, samples are flipped in  
220 up-down and left-right directions, each with a likelihood of 0.5. Fourth, samples are rotated by 0, 90, 180,  
221 or 270 degrees, each with a probability of 0.25. Fifth, samples are randomly shifted vertically and  
222 horizontally by -5 to 5 pixels. Sixth, the brightness of the sample image is adjusted by a random factor of  
223 -0.6 to +0.2, and the image contrast is randomly adjusted by -0.2 to 0.2. Seventh, the binary target bow  
224 echo masks are multiplied by 0.9, and random noise drawn from a uniform distribution between 0 and 0.1  
225 is added. This is known as “soft labels.” Lastly, both positive and negative samples are blended with  
226 randomly selected negative samples by taking the pixel-wise maximum reflectivity values of the two  
227 samples with a 0.5 likelihood. This last data augmentation is unusual but works well in our application  
228 because a) reflectivity features typically occupy only a fraction of the sample area, with most pixels being  
229 clear-sky and b) bow echoes are high-reflectivity features. When the last data augmentation is applied to a  
230 positive sample, the resulting image will typically still contain a bow echo that matches the target mask  
231 well.



## 232 **3.2 Training of U-Net 3+ CNN**

233 Our final semantic segmentation CNN model (Figure 3) uses the U-Net 3+ architecture (Huang et  
234 al., 2020). U-Net 3+ is a modern variant of the U-Net architecture (Ronneberger et al., 2015) and differs  
235 from the U-Net primarily in the addition of many more skip connections and its multi-resolution loss,  
236 which computes loss on rescaled classification masks generated from feature representations at various  
237 model levels.

238 U-Net models were originally developed for the segmentation of biomedical imagery but have been  
239 applied to image segmentation problems in other fields and are broadly useful for any image-to-image  
240 mapping tasks where the input and target data are the same (or similar) size and shape and merging multi-  
241 resolution information from the input data is important. U-Net CNNs have been applied to a myriad of  
242 problems in the atmospheric sciences, such as segmentation (Galea et al., 2024; Kumler-Bonfanti et al.,  
243 2020), super resolution (Geiss and Hardin, 2020; White et al., 2024), physics parameterization  
244 (Lagerquist et al., 2021), downscaling (Sha et al., 2020), and weather forecasting (Weyn et al., 2021).  
245 Perhaps most closely related to this study is Mounier et al. (2022), who used a U-Net to detect bow  
246 echoes in simulated radar reflectivity images from a forecast model. A U-Net is an appropriate choice for  
247 the segmentation of bow echoes because merging multi-resolution information is crucial for identifying  
248 the feature. For example, bow echoes have high reflectivity at the pixel scale, strong reflectivity gradients  
249 in the transverse direction at the mid-scale (tens of pixels), and the characteristic bow shape at the large  
250 scale (hundreds of pixels).



251  
252 Figure 3. A diagram of our semantic segmentation CNN architecture. The CNN inputs a 384×384-pixel radar  
253 image ( $Z_{Hmax}$  scaled to 0-255) and outputs a bow echo mask of the same size. The blue ovals represent 3×3  
254 convolutional layers, each followed by a batch normalization layer and a leaky rectified linear unit (ReLU)  
255 activation function. The first number in each blue oval indicates the spatial size (for both the width and height)  
256 of the output tensor, and the second represents the number of output channels. The solid arrows indicate  
257 connections in a standard U-Net architecture, with the downward arrows corresponding to 2×2 max-pooling  
258 and the upward arrows corresponding to 2×2 bilinear upsampling operations. The dashed lines represent the  
259 skip connections introduced in the U-Net 3+ architecture. These skip connections use max-pooling for spatial  
260 downsampling and bilinear interpolation for upsampling, followed by a 16-channel 3×3 convolutional layer  
261 with a linear activation. Layers with multiple inputs use channel-wise concatenation to combine those inputs.  
262 During training, the output tensors from the layers in the upsampling branch (blue ovals with red boundaries)  
263 are scaled to the output spatial resolution and passed through a 1-channel 1×1 convolutional layer with sigmoid  
264 activation. Training loss is computed on all 6 of the resulting masks. At inference time, only the mask  
265 outputted from the upper-rightmost layer is used.

266 Our U-Net 3+ CNN ingests 384×384-pixel  $Z_{Hmax}$  images where  $Z_{Hmax}$  have been clipped to a 0-  
267 50dBZ range and then linearly mapped to a range of 0-255. It is trained using binary cross entropy loss on  
268 masks generated from its 384, 192, 96, 48, 24, and 12-pixel resolution feature representations (Huang et  
269 al., 2020), though only the full-resolution (384×384-pixel) output mask is used at inference time. A  
270 detailed diagram of the model architecture is shown in Figure 3. Notably, although the model is trained  
271 using 384×384-pixel samples, it is a fully convolutional model and can process inputs of variable sizes.

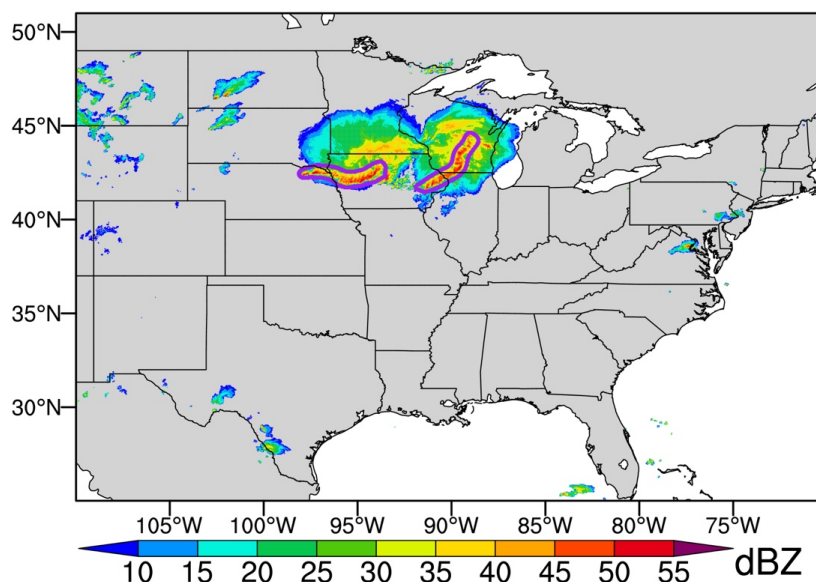
272 We use the Adam optimizer (Kingma and Ba, 2014) with the Keras default settings (Ketkar, 2017)  
273 and an initial learning rate of 0.001 for training. The U-Net 3+ CNN is first trained for 60 epochs  
274 composed of 1000 randomly generated training batches of 8 samples each. Then, we decrease the learning



275 rate to 0.0001 and train the CNN for an additional 20 epochs. The training duration is determined by  
276 performing an initial 5 rounds of training with 5-fold cross-validation and approximating the epoch  
277 numbers to reduce the learning rate and stop training when the mean intersection over union metric  
278 plateaus for the validation set. Instead of random shuffling, the validation sets are separated from the  
279 training dataset in temporally contiguous chunks to avoid any overlap because, sometimes, multiple  
280 samples may be drawn from different times of the same convective system.

### 281 3.3 Evaluation of the Semantic Segmentation CNN

282 We apply the trained U-Net 3+ CNN to the entire  $Z_{Hmax}$  dataset and obtain potential bow echo masks  
283 over the United States between 2004 and 2021 (Figure 4). As a final post-processing step, we ignore  
284 “bow echo” masks with less than 20 pixels ( $\sim 320 \text{ km}^2$ ), which are too small to be classified as bow  
285 echoes.



286  
287 Figure 4. Examples of the U-Net 3+ CNN identified bow echoes (purple contours) based on  $Z_{Hmax}$  (color  
288 shading) at 5:00 UTC on 17 June 2014.



289 Instead of validating our segmentation model at a pixel scale, as during the training stage, we prefer  
290 evaluating its performance in detecting bulk bow echo features. In other words, we care about whether the  
291 segmentation model can recognize the existence of bow echoes and capture their rough locations. Minor  
292 spatial biases in bow echo coverage do not affect our below derecho identification, which contains  
293 various flexible criteria to minimize their impacts, such as the buffer zone within 100 km of bow echoes.  
294 We also choose to validate the segmentation CNN specifically on MCS events where high reflectivity  
295 features are present. Identifying low-reflectivity and clear-sky images as non-bow echoes is desirable for  
296 our segmentation model but trivial and not of particular interest for creating a derecho climatology.

297 To build a testing dataset, we randomly select 217 MCS-associated  $Z_{Hmax}$  images in 2010 based on  
298 the following requirements. Each image is from a different MCS event. The images have variable sizes  
299 and contain the full spatial extents of the MCSs at the selected times; however, they must be at least  
300 192x192 pixels and cannot be drawn from a day that also has a sample in the training dataset. Three of the  
301 authors independently assessed the presence of bow echoes in each image, the results of which are then  
302 compared to the segmentation CNN (Table 1). Overall, the CNN model identifies 57 bow echoes, while  
303 human labelers 1, 2, and 3 identify 46, 76, and 66, respectively. The average human-human agreement  
304 and  $F_1$  scores are 82% and 0.69, while the average human-CNN agreement and  $F_1$  scores are 82% and  
305 0.67 (Table 1). The test indicates that, on the one hand, the detection of bow echoes in radar images is  
306 prone to subjective bias; on the other hand, the performance of the segmentation CNN is comparable to  
307 that of a human in identifying bow echoes. We emphasize that the CNN bow echo identification is only  
308 one component in our following derecho detection criteria, and the adverse impact of this uncertainty is  
309 mitigated by other constraints (e.g., almost continuous bow echo existence and strong gusts in proximity  
310 with bow echoes).

311 Table 1 Evaluation of the performance of the segmentation CNN in the bow echo identification<sup>1</sup>

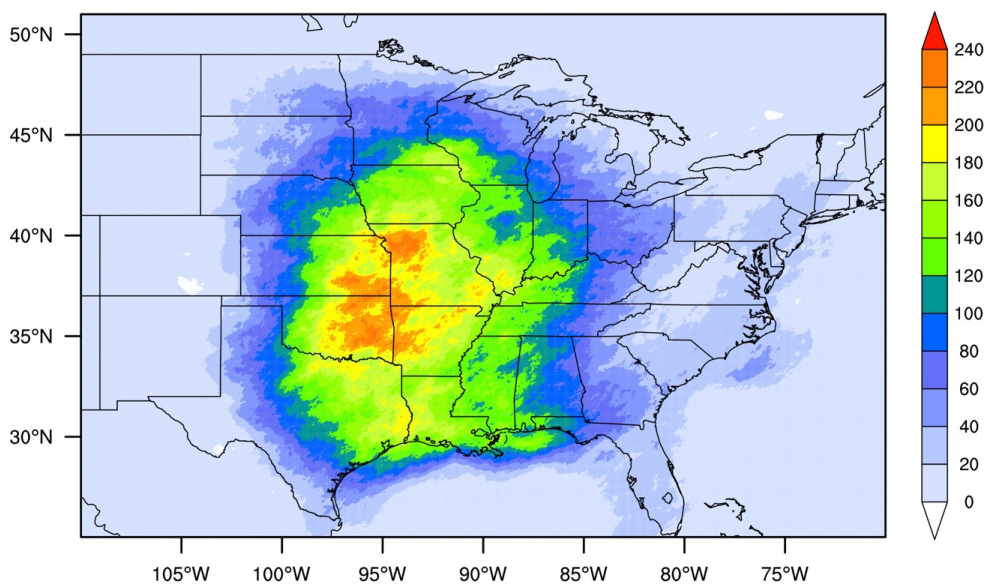
	CNN (57 <sup>2</sup> )	Person 1 (46)	Person 2 (76)	Person 3 (66)
CNN		84%	79%	83%
Person 1	0.66		77%	88%



Person 2	0.66	0.59		81%
Person 3	0.70	0.77	0.70	

312 <sup>1</sup>The upper part of the table shows agreement between two independent identifications ( $Agreement =$   
 313  $\frac{TP+TN}{TP+TN+FP+FN}$ ), and the lower part shows  $F_1$  scores ( $F_1 = \frac{2TP}{2TP+FP+FN}$ ), which is a better indication of the  
 314 ability to agree on positives when positives are a minority (Taha and Hanbury, 2015). Here,  $TP$  denotes true  
 315 positive,  $TN$  refers to true negative,  $FP$  is false positive, and  $FN$  is false negative. Notably, for the comparison  
 316 between any two independent identifications, we consider one as “true” and evaluate the other against it (and  
 317 which set of classifications are considered true does not impact these two metrics).  
 318 <sup>2</sup>The number of identified bow echoes from the 217 images.

319 We match the segmentation CNN detected bow echoes with MCS events from the MCS dataset and  
 320 identify those MCS-associated bow echoes, which are used to identify derechos in the following section.  
 321 Figure 5 shows the spatial distribution of MCS-associated bow echo occurrences from 2004 to 2021,  
 322 which is similar to the MCS spatial distribution with more occurrences in the Great Plains (Li et al.,  
 323 2021).



324 Figure 5. Spatial distribution of the number of MCS-associated bow echoes from 2004 to 2021. Here, we use  
 325 bow echo masks produced by the segmentation CNN and exclude bow echoes that do not overlap with MCS  
 326 events. Notably, the PyFELXTRKR-generated MCS dataset contains tropical cyclones (TCs). This figure  
 327 excludes bow echoes from those non-derecho MCS events that overlap with TCs from the International Best  
 328 Track Archive for Climate Stewardship (IBTrACS) Version 4 data over the North Atlantic basin (Knapp et al.,  
 329 2010) following the approach of (Feng et al., 2021).  
 330



## 331 4 Derecho identification

332 As mentioned above, we adopt the derecho definition proposed by Corfidi et al. (2016) but revise  
333 some criteria based on previous studies (Johns and Hirt, 1987; Bentley and Mote, 1998) and the limitation  
334 of the observational datasets used in this study so that they can be used in the objective identification of  
335 derechos. Our detailed definition criteria are summarized below.

336 1) A derecho must be attached to an MCS from the MCS dataset. This is the most straightforward  
337 requirement and one of our advantages. Due to the lack of a reliable MCS dataset, most previous  
338 studies spent much effort identifying spatiotemporally continuously propagating convective  
339 systems (Squitieri et al., 2023).

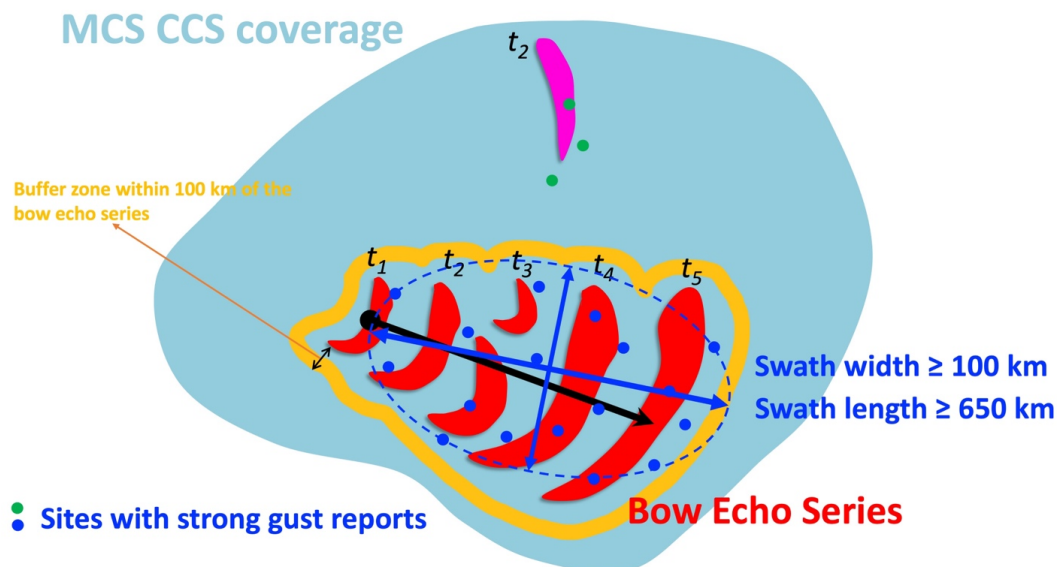
340 2) At least one derecho feature (DF) exists in the MCS lifetime. A DF is defined as a continuous  
341 period satisfying the following criteria (Figure 6).

342 2.1) The DF must last for at least 2 hours, and bow echo occurs during  $\geq 80\%$  of the DF period.

343 For example, if the DF lasts for 10 hours, it must have bow echoes in at least 8 hours. In  
344 addition, no more than 2 hours can elapse between successive bow echo occurrences. In other  
345 words, bow echo must exist for at least one hour in any two consecutive hours. The above two  
346 thresholds consider the segmentation CNN identification uncertainty and the diversity of MCS  
347 events. Moreover, a DF requires these bow echoes to be from the same bow echo series. Due to  
348 merging or splitting or the complex nature of some convective systems, a bow echo at one hour  
349 may be far from the bow echoes right after or before that hour or another bow echo during that  
350 hour (Figure 6). In such a rare situation, these bow echoes are unlikely caused by the same  
351 physical process and, therefore, do not belong to the same bow echo series. We separate  
352 different bow echo series in two steps. First, a distance criterion categorizes multiple bow echoes  
353 in the same hour into different series. Any bow echoes more than 100 km from each other  
354 belong to different series. Second, we temporally connect bow echoes from the same series using



355 another distance threshold. The distance between two successive bow echoes (no more than 2  
356 hours can elapse between their occurrences) from the same series must be no more than 200 km.  
357 Notably, the second step can overwrite the first step. For example, two bow echoes at hour  $t$   
358 belong to different series in the first step, but in the second step, they are close enough ( $\leq 200$   
359 km) to the same bow echo at hour  $t-1$ . If so, they are considered from the same bow echo series.



360 Figure 6. Schematic of the automated detection algorithm. Red and pink contours represent bow echoes. At  
361 time  $t_2$ , there are two bow echoes belonging to different bow echo series due to their great distance from each  
362 other. In contrast, the two bow echoes at  $t_3$  are from the same bow echo series since they are close to each  
363 other. The pink bow echo at  $t_2$  is far from the bow echoes at  $t_1$  and  $t_3$ . Therefore, they belong to different bow  
364 echo series. The sites (green dots) with strong gust reports outside the 100-km buffer zone of the bow echo  
365 series (i.e., the DF area) are excluded from the strong gust swath calculation. The black arrow indicates the  
366 propagation direction of the bow echo series.  
367

368 2.2) We calculate the DF-associated maximum gust speed for each land observational site during  
369 the DF period. Within 100 km of the DF bow echoes, which we name the DF area, there must be  
370  $\geq 10$  sites with strong gusts (gust speed  $\geq 17.43 \text{ m s}^{-1}$ ) and  $\geq 1$  site with damaging gusts (gust  
371 speed  $\geq 25.93 \text{ m s}^{-1}$ ). In addition, the fraction of sites with strong gusts should be  $\geq 20\%$ . This  
372 fraction criterion is intended to exclude potential MCSs associated with extratropical cyclones,  
373 which could produce strong or damaging gusts over limited observational sites but weaker gusts



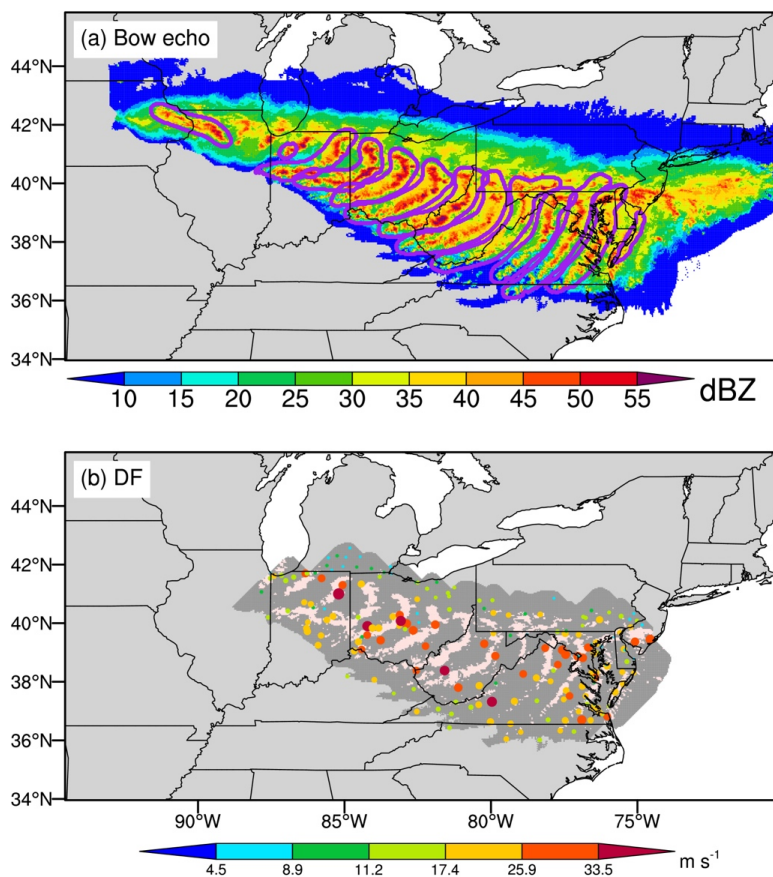
374 at most other sites. Besides, a DF requires that no more than 2 hours can elapse between  
375 successive strong gust reports. Then, we calculate the major and minor axis lengths of the fitted  
376 ellipse swath using the locations of those sites with strong gust reports (Figure 6). As a DF, the  
377 major and minor axis lengths must be at least 650 km and 100 km, respectively. We emphasize  
378 that our gust speed criteria are weaker than those of previous studies (Squitieri et al., 2023;  
379 Bentley and Mote, 1998; Johns and Hirt, 1987), which estimated the gust swath based on  
380 damaging gusts. Moreover, previous studies often required a few reports of gust speed  $\geq 33 \text{ m s}^{-1}$ .  
381 <sup>1</sup>. Notably, many gust speeds in earlier studies were from post-disaster estimates, while this  
382 study uses ISD surface station measurements. Post-disaster estimates can capture damaging gust  
383 occurrences over a much larger area. In contrast, due to the limited coverage of observational  
384 sites, real-time measurements may miss substantial damaging gust occurrences in nearby  
385 regions. Therefore, we lower the gust speed criteria to capture potential derechos.

386 2.3) If no DF is identified for a given MCS using the above procedures, we can relax the  
387 distance requirement in (2.2) to be within 200 km of the DF bow echoes that satisfy the  
388 condition that there is no bow echo from the same bow echo series an hour ago or later during  
389 the DF period. If the bow echo is in the first hour of the DF period and there are no CNN-  
390 identified bow echoes for the MCS event an hour ago, we can also extend the distance threshold  
391 to 200 km. This is similar to the bow echo in the last hour of the DF period but without any  
392 CNN-identified bow echoes an hour later. Notably, the distance extension is optional. For the  
393 bow echoes satisfying the above conditions, the distance threshold can be either 100 or 200 km.  
394 Using 100 km is superior to using 200 km until we find a DF if it exists. The distance extension  
395 is also intended to minimize the impacts of the bow echo identification error. If a bow echo is  
396 missed in the semantic segmentation procedure, extending the distance threshold can include  
397 strong gusts associated with the missed bow echo, thus slightly reducing the derecho detection  
398 error.



399 We identify 537 derechos between 2004 and 2021 using the above objective detection criteria, with  
400 an example of the June 2012 North American derecho shown in Figure 7. Figure 7a displays the CNN-  
401 identified bow echoes, and Figure 7b shows the DF area and associated gust speeds. As expected, the  
402 derecho produced extensive strong gusts during its DF period.

403 Although we have considered the segmentation CNN bow echo identification uncertainties in the  
404 above derecho definition criteria, there is no guarantee that every specific situation is considered.  
405 Therefore, we carefully examine all the identified derechos and remove 32 events that are possibly false  
406 detections primarily due to the false identification of bow echoes (Figure S3). In addition, we manually  
407 examine all MCS events (808 in total, excluding the aforementioned 537 automatically identified  
408 derechos) that produce extensive strong ( $\geq 10$  observational sites) and damaging ( $\geq 1$ ) gusts over land  
409 areas with a strong gust swath of at least  $650 \times 100 \text{ km}^2$ . Our manual examination focuses on bow echo  
410 identification errors but does not change any of the above derecho definition thresholds or parameters. For  
411 those MCSs (55 events in total) that are potential derechos based on our visual inspection, we manually  
412 label their bow echo occurrences that fail the segmentation identification during potential DF periods  
413 (Figure S4) and rerun the automated derecho detection algorithm. Finally, 51 events meet the derecho  
414 detection criteria described above.



415  
416 Figure 7. (a) Spatial evolution of  $Z_{Hmax}$  (color shading) and CNN-identified bow echoes (purple contours) from  
417 the June 2012 North American derecho. (b) Spatial evolution of the corresponding DF. The DF lasted from  
418 17:00 UTC on 29 June to 6:00 UTC on 30 June 2012. The misty rose shading in (b) corresponds to  $Z_{Hmax} \geq 40$   
419 dBZ, while the gray shading refers to the DF area. Colored dots are the same as those in Figure 1c, except only  
420 the DF-associated gust measurements are shown.

## 421 5 Dataset evaluation and uncertainty

422 Finally, we obtain 556 derechos between 2004 and 2021, 505 of which are identified automatically  
423 and 51 of which are added manually. The number of derechos (30.9 per year) is much larger than  
424 previous estimations (6.1-20.9 per year) using a major axis length threshold of 400 km (Squitieri et al.,  
425 2023; Johns and Hirt, 1987; Bentley and Mote, 1998; Evans and Doswell, 2001; Guastini and Bosart,  
426 2016; Ashley and Mote, 2005). The number is also much larger than the result of Corfidi et al. (2016),  
427 which identified only 25 derechos in the warm seasons during 2010-2014 using a major axis length



428 threshold of 650 km. The large discrepancies are likely related to our usage of strong gusts but not  
429 damaging gusts to calculate wind damage swath and other definition criteria. However, the diverse  
430 observational datasets used in the derecho detections also play a critical role. Previous studies did not  
431 have an available MCS dataset; as a result, many of their definition criteria were intended to capture MCS  
432 events. In contrast, we have developed a high-quality, high-resolution MCS tracking dataset using  
433 PyFLEXTKR and many coincident ground-based and remote-sensing observations. Our definition criteria  
434 purely focus on the derecho properties and generation mechanism. Previous studies may underestimate  
435 the derecho number due to missing MCS events. We confirm this by comparing the derechos from the  
436 NOAA SPC with our derecho dataset in 2004 and 2005 (Table 2). The NOAA SPC data  
437 (<https://www.spc.noaa.gov/misc/AbtDerechos/annualevents.htm>; last access: November 17, 2023).  
438 provide more detailed timings and locations of derechos in 2004 and 2005 than previous studies (Squitieri  
439 et al., 2023), which is the only available dataset that we can use to evaluate our derecho dataset at the  
440 event scale. Notably, the NOAA SPC data contains not only derechos but also convective windstorms of  
441 near-derecho size, and we do not know which event is a derecho or a convective windstorm of near-  
442 derecho size. In addition, the data is based on gust speed measurements and post-disaster estimations.  
443 There is not an underlying MCS dataset for the NOAA SPC data.

444 The NOAA SPC data contains 50 derechos and convective windstorms of near-derecho size, 22 of  
445 which are directly captured by the automated detection procedure, and 2 of which can be captured after  
446 we manually correct the segmentation CNN bow echo identification errors. Five of the 50 events are  
447 entirely missed in the MCS dataset, possibly because they move too fast and do not meet the  
448 PyFLEXTKR > 50% areal overlap tracking criterion using the hourly combined satellite and NEXRAD  
449 dataset, or they break other MCS requirements in PyFLEXTKR (Feng et al., 2019). We emphasize that  
450 10 of the 50 NOAA SPC events are not derechos based on the actual gust speed measurements since we  
451 do not find any land damaging gust reports associated with the MCS events. Seven of the 50 events are  
452 not derechos using the major axis length threshold of 650 km and the minor axis length threshold of 100



453 km, even if we consider all the observational sites associated with the events, regardless of whether they  
454 are in proximity with the bow echoes. One event is an extratropical cyclone. These 18 events are excluded  
455 from derechos using more objective or consistent criteria as NOAA SPC. The remaining three of the 50  
456 events are missed in our derecho dataset due to the criteria used in our derecho definition, two of which  
457 are due to too few sites with strong gusts, and one is due to the violation of the bow echo and gust speed  
458 criteria. In summary, after excluding those 18 non-derechos and the five missed events in the MCS  
459 dataset, the identification accuracy of our automated detection approach is  $\frac{22}{50-18-5} = 81\%$  (Table 2).  
460 Even if we consider the five missed MCS events, the accuracy can reach up to  $\frac{22}{50-18} = 69\%$ . For the final  
461 derecho dataset with the 51 manually added events, the accuracy is  $\frac{22+2}{50-18} = 75\%$ . Finally, our derecho  
462 dataset identifies 14 derechos that are entirely missed by NOAA SPC, confirming the underestimation of  
463 derecho numbers in previous studies due to the lack of a reliable MCS dataset (Squitieri et al., 2023).

464



**Table 2. Evaluation of our derecho dataset against the NOAA SPC data in 2004 and 2005**

	Year 2004	Year 2005	Sum
NOAA SPC <sup>1</sup>	24	26	50
Captured by our dataset	10	12	22
Events missed in the MCS dataset <sup>2</sup>	2	3	5
No land damaging gust, strong gust swath too small, no bow echo, or extratropical cyclone <sup>3</sup>	10	8	18
Bow echo identification error <sup>4</sup>	1	1	2
Other criteria not satisfied <sup>5</sup>	1	2	3
Our identified derechos not listed by NOAA SPC	5	9	14
Identification accuracy if excluding those missed MCS events <sup>6</sup>	83%	80%	81%
Identification accuracy if including those missed MCS events <sup>7</sup>	71%	67%	69%

<sup>1</sup>NOAA SPC provides the tracks of derechos and other convective systems of near derecho size in 2004 and 2005.  
<sup>2</sup>Some events were moving so fast that the PyFLEXTRKR algorithm, which tracks storms with spatial overlapping > 50%, could not track the systems with the hourly combined satellite and NEXRAD dataset, while some may not meet other MCS criteria.  
<sup>3</sup>Here, “strong gust swath too small” refers to those MCS events with the largest strong gust swath of less than 650 km × 100 km, even if we include those strong gusts not associated with bow echoes.  
<sup>4</sup>It refers to those MCS events with bow echoes not captured by the segmentation CNN. If we manually label the missed bow echoes, they would be identified as derechos.  
<sup>5</sup>It refers to MCS events that do not meet any other criteria (e.g., too few sites with strong gusts) and cannot be classified as derechos.  
<sup>6</sup> $Accuracy = \frac{Captured\ by\ our\ dataset + Bow\ echo\ identification\ error + Other\ criteria\ not\ satisfied}{Captured\ by\ our\ dataset}$   
<sup>7</sup> $Accuracy = \frac{Captured\ by\ our\ dataset + Bow\ echo\ identification\ error + Other\ criteria\ not\ satisfied + MCS\ events\ missed\ in\ the\ MCS\ dataset}{Captured\ by\ our\ dataset + Bow\ echo\ identification\ error + Other\ criteria\ not\ satisfied + MCS\ events\ missed\ in\ the\ MCS\ dataset}$

465

466  
 467  
 468  
 469  
 470  
 471  
 472  
 473  
 474  
 475  
 476



477           Although the evaluation against the NOAA SPC data indicates the high quality of our derecho  
478 dataset, we must acknowledge its uncertainties caused by several sources.

479           The first uncertainty source is from the MCS dataset, as mentioned in the evaluation against the  
480 NOAA SPC data. The areal overlap threshold, which is set to 50% and used to connect consecutive CCSs  
481 in the current PyFLEXTRKR configuration, cannot capture those very fast-moving convective systems  
482 with the hourly satellite and NEXRAD datasets. Reducing the threshold will undoubtedly increase the  
483 “MCS” and then the “derecho” number, but it may also increase the number of false tracks that do not  
484 belong to the same type of storm. The threshold of 50% is widely used in the different versions of the  
485 FLEXTRKR algorithms (Li et al., 2021; Feng et al., 2023; Feng et al., 2019) and other tracking  
486 algorithms based on overlap (e.g., (Whitehall et al., 2015)). Therefore, we would like to keep the overlap  
487 threshold as is, but users should realize the uncertainties of the MCS dataset caused by many adjustable  
488 parameters (e.g., area overlap threshold, MCS duration, and major axis length) and the limitations of the  
489 observational datasets used in PyFLEXTRKR (Feng et al., 2019; Li et al., 2021).

490           The second uncertainty source is related to the segmentation CNN identification of bow echoes.  
491 Although the evaluation in Section 3.3 shows the high accuracy of our bow echo identification and we  
492 consider the bow echo identification uncertainties in the automated derecho detection procedure, we still  
493 miss a small fraction of derechos and falsely classify some non-derechos as derechos due to the bow echo  
494 identification error. To alleviate the CNN identification errors, we spend much effort manually examining  
495 the derecho events identified by the automated algorithm and other MCS events that produce widespread  
496 strong gusts. However, the manual examination is susceptible to subjective biases, and it is difficult to  
497 completely eliminate the bow echo identification uncertainties.

498           The third uncertainty source is from the gust speed measurements. Although we only use gust  
499 measurements passing the ISD quality control, it is not guaranteed that all gust speeds are reliable and  
500 have the same quality, such as the site we exclude in Section 2.2 due to its unrealistic number of



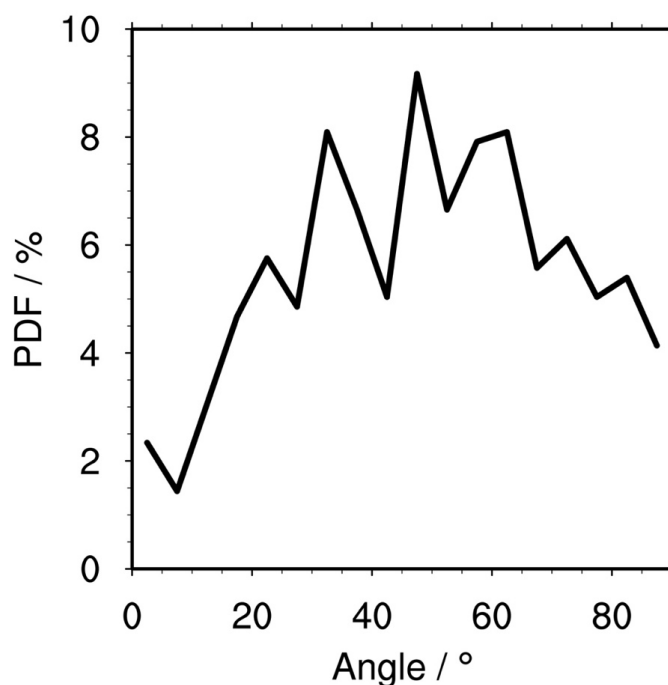
501 damaging gust reports. Moreover, we cannot qualitatively evaluate the impact of the gust measurement  
502 uncertainty on the derecho dataset, but users should be aware of the limitations of the gust speed  
503 observations.

504 The last uncertainty source is related to the derecho definition criteria. Many adjustable parameters  
505 and procedures are used in our algorithm to detect derechos. There is no doubt that changing these  
506 parameters will alter the identified derecho number. For example, if we change the major axis length  
507 threshold of the strong gust swath to 400 km, the derecho number will increase to 654 (a 29.5% increase).  
508 As the first climatological derecho dataset that utilizes bow echoes in the derecho identification and  
509 provides detailed tracking for each event, evaluating the uncertainties of the tunable parameters is  
510 unfeasible and not our priority either. However, based on our sensitivity tests, the derecho spatial  
511 distribution and seasonal variation patterns in Section 6 generally stay mostly the same with different  
512 parameters (e.g., reducing the strong gust fraction threshold to 10% or the threshold of the number of sites  
513 with strong gust reports to 5). The exception is that when we calculate the gust swath length and width  
514 using sites (requiring  $\geq 10$  sites) with damaging gusts as in previous studies (Squitieri et al., 2023), the  
515 derecho number is significantly reduced to 19, highlighting the spatial limitation of ISD gust  
516 measurements. We emphasize that although our derecho definition follows Corfidi et al. (2016), we  
517 exclude the “forward propagating” criterion they proposed. We try several methods to calculate the angles  
518 between the derecho orientations and their propagation directions but cannot obtain satisfying and  
519 accurate results for some events with complex structures. Figure 8 shows the probability density function  
520 (PDF) of the angles between “derecho propagation directions” and “bow echo orientations” for all  
521 derechos from the final derecho dataset. Based on this type of calculation, 78% of derechos have an angle  
522  $\geq 30^\circ$ , and 58% of derechos have an angle  $\geq 45^\circ$ . For those derechos with angles  $< 30^\circ$ , it does not mean  
523 that they are not forward propagating systems, but it is more likely that this type of angle calculation does  
524 not reflect their actual propagation direction. In total, even though we do not use the “forward



525 propagating” criterion in the derecho definition, most of the identified derechos are indeed forward  
526 propagating systems.

527 Finally, users should acknowledge the high quality of our derecho dataset but understand its  
528 limitations due to various uncertainties during its generation.



529  
530 Figure 8. The probability density function (PDF) of the angles between derecho propagation directions and  
531 bow echo orientations. For any derecho, we calculate all the bow echoes' orientations during its DF period and  
532 use the median orientation in the angle calculation. Propagation direction is also based on bow echoes during  
533 the DF period. We select any two distinct bow echoes during the period and use their centroid points to derive  
534 a direction. If there are  $n$  bow echoes, we can obtain  $C_n^2 = \frac{n \times (n-1)}{2}$  directions. Similarly, we use the median  
535 direction as the derecho's propagation direction to calculate the angle. The angle is initially in the range of -  
536  $180^\circ$  to  $180^\circ$ , and we adjust them to be between  $0^\circ$  and  $90^\circ$  to reflect the minimum angle between the  
537 derecho's orientation and propagation direction.

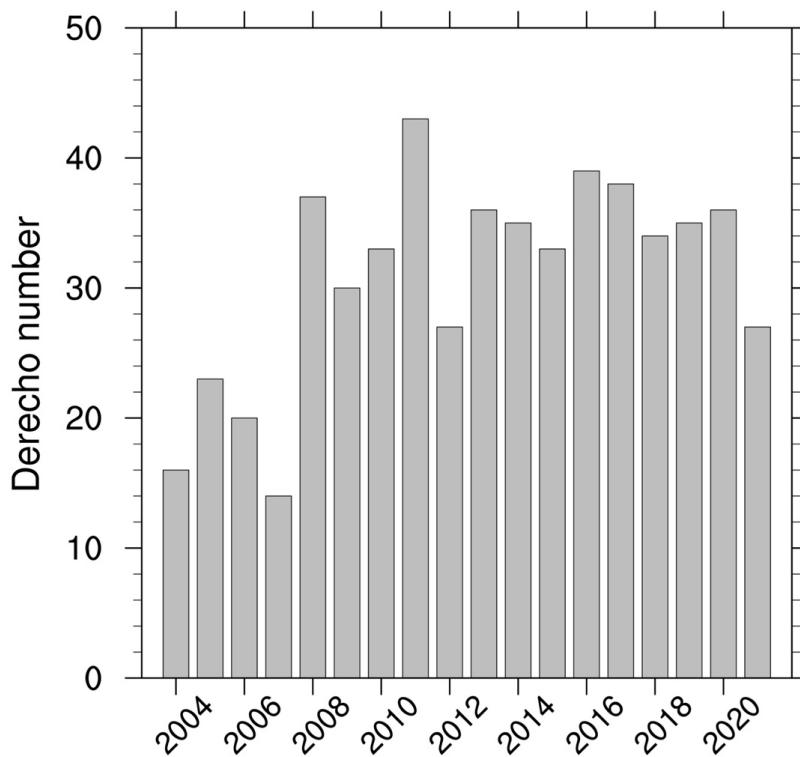
## 538 **6 Derecho climatological characteristics**

539 We use the final derecho dataset with 556 derechos to conduct the following climatological analyses.

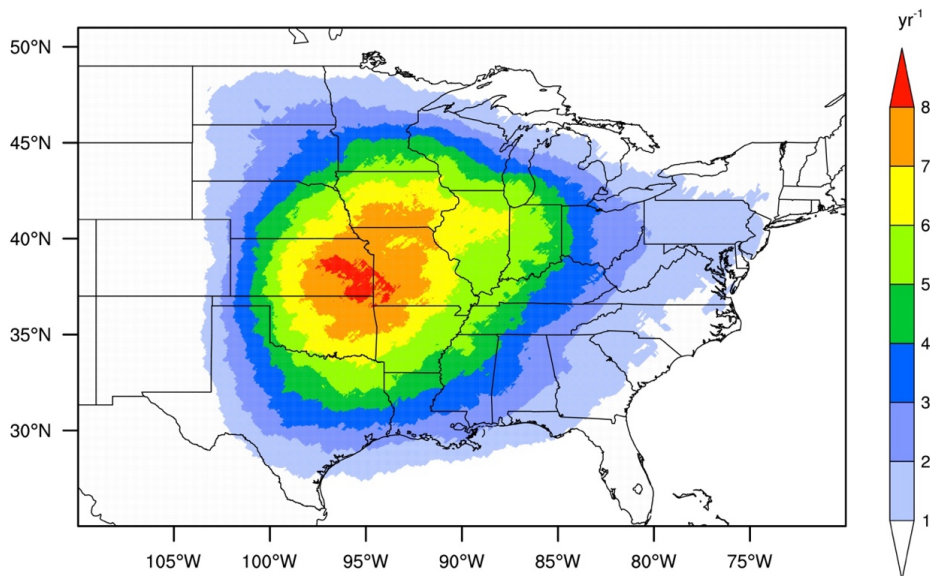


## 540 **6.1 Annual statistics**

541 Figure 9 displays the annual derecho numbers from 2004 to 2021. There is an apparent jump in the  
542 derecho number before (~20 derechos per year) and after 2007 (~30 derechos per year), which may be  
543 partially related to the general increase in the number of gust speed observational sites from 2004 to 2010  
544 (Figure S5). Figure 10 shows the spatial distribution of yearly averaged annual derecho numbers between  
545 2004 and 2021, and the derecho paths during their DF periods are displayed in Figure S6. The central  
546 Great Plains has the most frequent derecho occurrences, extending to Oklahoma in the south, Iowa in the  
547 north, Kansas in the west, and Illinois in the east. The areas with frequent derecho occurrences are  
548 generally consistent with previous studies (Coniglio and Stensrud, 2004; Guastini and Bosart, 2016; Johns  
549 and Hirt, 1987; Ashley and Mote, 2005), although some differences are identified. For example, several  
550 studies identified a northwest-southeast axis with frequent derecho occurrences extending from southern  
551 Minnesota to Ohio, which is not apparent in our spatial distribution (Johns and Hirt, 1987; Coniglio and  
552 Stensrud, 2004; Guastini and Bosart, 2016). The differences can be caused by many factors, such as  
553 distinct derecho definitions and observational datasets used in these studies. We make a sensitivity test by  
554 calculating the gust swath using  $\geq 10$  sites with damaging gusts as mentioned in Section 5, which  
555 identifies 19 derechos. The corresponding spatial distribution in Figure S7 well captures the  
556 aforementioned west-east axis, although the occurrence frequency is much smaller than in previous  
557 studies with more than one derecho occurrence per year (Johns and Hirt, 1987; Coniglio and Stensrud,  
558 2004; Guastini and Bosart, 2016). The sensitivity test seems to indicate that the most intense derechos  
559 prefer to occur in the northern Great Plains and Midwest, while weaker derechos occur preferably in  
560 central Great Plains around the junction of Oklahoma, Kansas, Missouri, and Arkansas.



561  
562 Figure 9. Bar chart of the annual derecho numbers from 2004 to 2021.



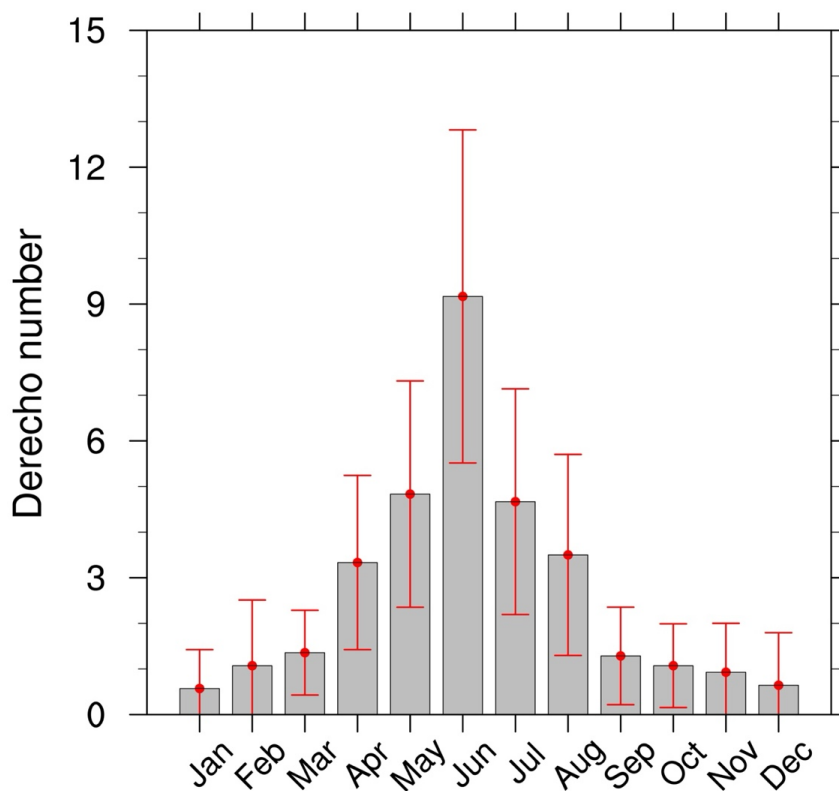
563  
564 Figure 10. Spatial distribution of yearly averaged annual derecho numbers over the United States  
565 east of the Rocky Mountains between 2004 and 2021. Here, we use derecho DF areas as derecho spatial coverages.



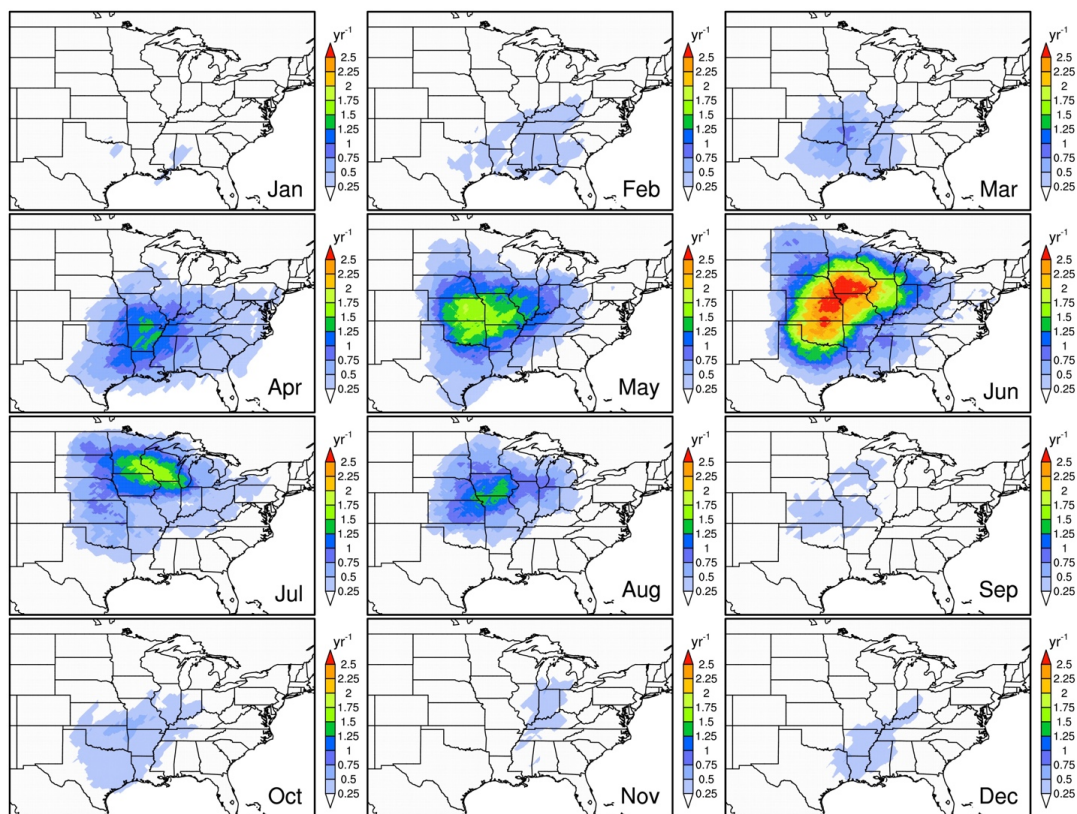
## 566 **6.2 Monthly statistics**

567 Figure 11 displays the yearly averaged seasonal variations in the derecho number, with remarkably  
568 more derechos in the warm than cold seasons, a feature widely captured by previous studies (Ashley and  
569 Mote, 2005; Squitieri et al., 2023; Bentley and Sparks, 2003). The derecho seasonal variation resembles  
570 that of the MCS events (Feng et al., 2019), similar to the derecho annual spatial distribution (Figure 10  
571 and Feng et al. (2019)).

572 Figure 12 shows the spatial distributions of the yearly averaged monthly derecho numbers between  
573 2004 and 2021. On the one hand, many more derechos occur in the warm than cold months. On the other  
574 hand, we find remarkable shifts in the areas with the most frequent derecho occurrences from April to  
575 August. The region with the most derechos moves northward during the warm season but shrinks zonally.  
576 The northward shifts also resemble the MCS events (Li et al., 2021). We can identify two axes with  
577 frequent derecho occurrences. One is in the south-north direction along the Great Plains, and the other is  
578 in the west-east direction along the northern Great Plains and Midwest, which are consistent with the  
579 derecho paths in Figure S6. The axes may represent the two types (serial and progressive) of derechos  
580 mentioned in Squitieri et al. (2023). A follow-up study will be conducted to investigate the large-scale  
581 environmental conditions associated with different types of derechos based on the developed derecho  
582 dataset. Notably, derechos are concentrated in the Lower Mississippi Valley in the cold season, which is  
583 also consistent with previous studies (Squitieri et al., 2023).



584  
585 Figure 11. Yearly averaged monthly variations of the derecho numbers between 2004 and 2021. The error bars  
586 denote standard deviations.



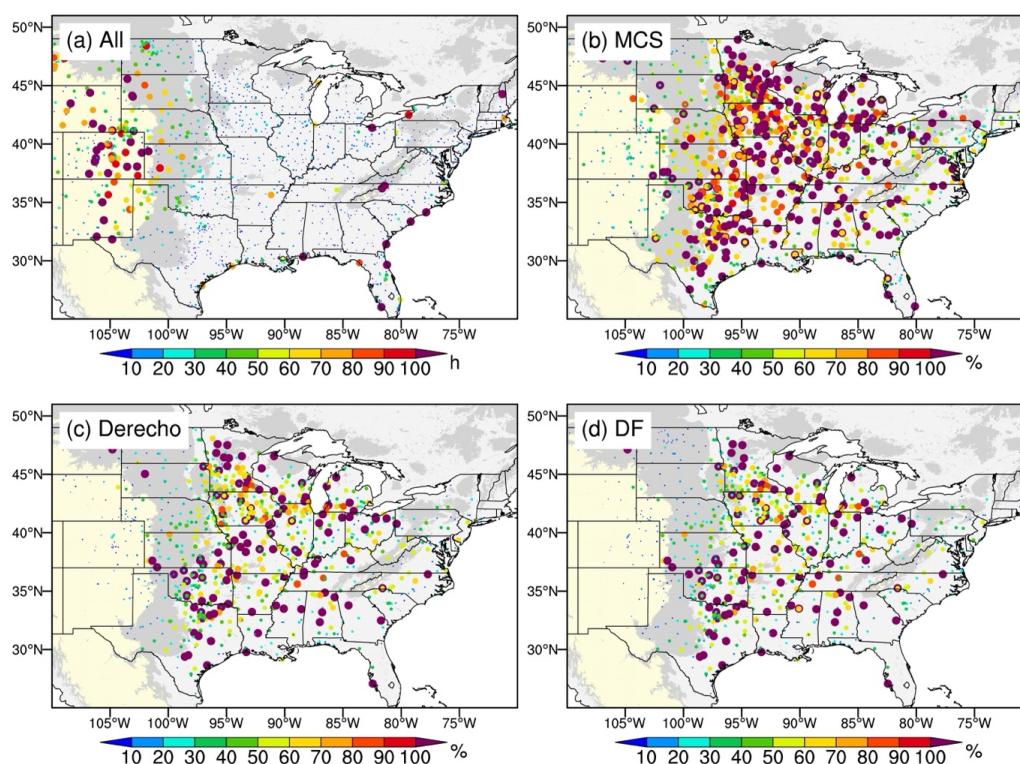
587  
588 Figure 12. Same as Figure 10 but for yearly averaged monthly derecho numbers over 2014-2021.

### 589 6.3 Wind damage characteristics

590 We examine the contributions of derechos and DFs to all the damaging gust reports in the United  
591 States area of the dataset domain between 2004 and 2021 in Figures 13, S2, and S8. MCSs contribute  
592 about 36.8% of the damaging gust reports, but most occur east of the Rocky Mountains. On average,  
593 derechos and DFs contribute 19.2% and 16.5% of the damaging gust occurrences, respectively. In other  
594 words, about half of the damaging gusts associated with MCS events are related to derechos.  
595 Understanding the underlying mechanisms will be our focus in a follow-up study. In addition, most (>  
596 80%) derecho-generated damaging gusts occur during the DF periods, justifying using DF in our derecho  
597 definition, consistent with the larger probabilities of extreme gusts in the gust speed PDF of DFs than that



598 of derechos in Figure S9. The gust speed PDFs for MCSs and derechos indicate that derechos are more  
599 favorable for producing extreme gusts than MCSs (Figure S9). Moreover, as expected, the contributions  
600 of derechos to damaging gust reports are the highest in the Great Plains, Midwest, and Lower Mississippi  
601 Valley (Figure 13).



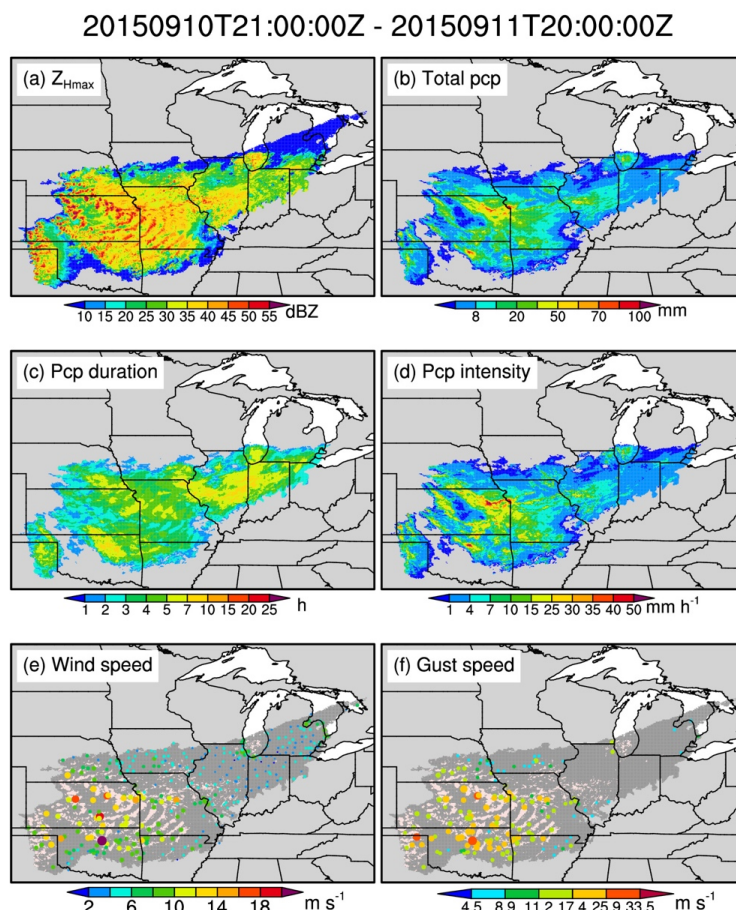
602  
603 Figure 13. (a) The total numbers of damaging gust occurrences between 2004 and 2021 at weather stations  
604 over the United States east of the Rocky Mountains. (b) Relative contributions of MCS events to the damaging  
605 gust occurrences in (a). (c) is the same as (b) but for relative contributions of derechos. (d) is the same as (c),  
606 but we only consider the DF periods when counting the derecho-associated damaging gust occurrences.  
607 Similar to Figure 5, we exclude non-derecho MCS events overlapping with TCs in (b). The dot sizes are  
608 proportional to the corresponding values. Light-yellow shading denotes an elevation greater than 1000 m;  
609 light-gray shading denotes an elevation between 400 m and 1000 m; and smoke-white shading denotes an  
610 elevation less than 400 m. Background white is for oceans and lakes.



## 611 **7 Data availability**

612 The final derecho dataset and the corresponding user guide are available  
613 at <https://doi.org/10.5281/zenodo.10884046> (Li et al., 2024). The original format of the data files is  
614 NetCDF-4, and we compress them for each year so that the dataset is easily accessible. The user guide  
615 contains a detailed description of the data files to help users understand the dataset. For each derecho, the  
616 dataset provides two figures displaying the temporal evolutions of  $Z_{Hmax}$ , precipitation, wind speed, and  
617 gust speed during its entire lifetime and DF period (e.g., Figures 14 and S10). The figures are helpful for  
618 users to understand the basic characteristics of the derechos immediately. Notably, the dataset contains all  
619 the derecho-associated gust speed measurements, so users can further separate the derechos into different  
620 intensities, as in Coniglio and Stensrud (2004).

621



622  
623 Figure 14. Similar to Figure 1 but for the spatial evolutions of (a)  $Z_{Hmax}$ , (b) total accumulated precipitation, (c)  
624 precipitation duration, (d) mean precipitation intensity, (e) hourly maximum wind speed, and (f) hourly  
625 maximum gust speed during the entire lifetime of a derecho that occurred on 10-11 September 2015. In (e) and  
626 (f), the misty rose shading corresponds to areas with  $Z_{Hmax} \geq 40$  dBZ, and the dark gray shading refers to  
627 derecho coverage with  $Z_{Hmax} < 40$  dBZ. The figure title refers to the derecho timing range.

## 628 8 Conclusions

629 This study presents a high-resolution (4 km and hourly) observational derecho dataset covering the  
630 United States east of the Rocky Mountains from 2004 to 2021. We develop the dataset using an MCS  
631 dataset generated by the PyFLEXTRKR software, a machine-learning-based identification of bow echoes,  
632 ISD hourly gust speed measurements, and physically based identification criteria. The evaluation and  
633 potential uncertainties of the dataset are discussed. The dataset contains 556 derechos, most of which are



634 in the warm season (April-August). Analyses indicate that derechos preferably occur in the Great Plains  
635 and Midwest. Areas with the most frequent derechos show a northeastward shift from April to August.  
636 Derechos contribute 19.2% of land damaging gusts over the United States between 2004 and 2021. About  
637 half of MCS-associated damaging gusts are produced by derechos. As the first derecho dataset that uses  
638 machine-learning identification of bow echoes, physically based definition criteria, and surface station  
639 measured gust speeds, it provides an independent reference for derecho climatology compared to previous  
640 studies. In addition, the derecho dataset can be used to investigate the derecho initiation and development  
641 mechanisms, the environments that facilitate the formation and intensification of derechos, and the  
642 damage of derechos to human security and property. Moreover, due to its high spatiotemporal resolutions,  
643 the dataset can be used to select specific derecho events for case studies and evaluate the numerical model  
644 simulations.

## 645 **Author Contributions**

646 JL, ZF, and LRL designed the study. JL prepared the input files for PyFLEXTRKR, and ZF ran  
647 PyFLEXTRKR to generate the MCS dataset. JL and ZF generated the initial positive and negative bow  
648 echo samples. AG trained and validated the CNN model. AG applied the trained semantic segmentation  
649 CNN to identify bow echoes from the MCS dataset with discussions with JL and ZF. JL defined and  
650 identified derechos with discussions with ZF. JL evaluated the derecho dataset and manually examined  
651 the data. JL analyzed the derecho climatology with discussions with ZF. JL wrote the manuscript except  
652 for the machine-learning part which was written by AG. All co-authors reviewed the manuscript.

## 653 **Competing Interests**

654 The authors declare that they have no conflict of interest.



## 655 **Acknowledgments**

656 The NOAA SPC derechos and near-derechos are available at  
657 <https://www.spc.noaa.gov/misc/AbtDerechos/annualevents.htm> (last access: November 17, 2023). The  
658 named derechos we use to generate bow echo samples are from  
659 [https://en.wikipedia.org/wiki/List\\_of\\_derecho\\_events](https://en.wikipedia.org/wiki/List_of_derecho_events) (last access: 19 March 2023). The elevation data is  
660 from <http://iridl.ldeo.columbia.edu/SOURCES/.NOAA/.NGDC/.GLOBE/> (last access: March 7, 2024).  
661 The IBTrACS Version 4 TC data over the North Atlantic basin is from [https://doi.org/10.25921/82ty-](https://doi.org/10.25921/82ty-9e16)  
662 [9e16](https://doi.org/10.25921/82ty-9e16) (Knapp et al., 2018). Thank Drs. Israel L. Jirak, Brian J. Squitieri, and Andrew R. Wade from  
663 NOAA SPC for discussing the derecho definition criteria with us.

664 The bow echo segmentation code and datasets are available at <https://doi.org/10.5281/zenodo.10822721>  
665 (Geiss et al., 2024). This repository includes the trained CNN weights and instructions for use. A video  
666 supplement showing the bow echo segmentation scheme in use can be viewed at  
667 [https://youtu.be/iHWY\\_OhaVUo](https://youtu.be/iHWY_OhaVUo) and is permanently archived in the above Zenodo repository.

## 668 **Financial support**

669 This research is supported by the Regional and Global Model Analysis and Multisector Dynamics  
670 program areas of the U.S. Department of Energy Office of Science Biological and Environmental  
671 Research as part of the HyperFACETS project. PNNL is operated for the Department of Energy by  
672 Battelle Memorial Institute under Contract DE-AC05-76RL01830.

673



## 674 References

- 675 Adams-Selin, R. D. and Johnson, R. H.: Mesoscale surface pressure and temperature features associated with  
676 bow echoes, *Monthly weather review*, 138, 212-227, <https://doi.org/10.1175/2009MWR2892.1>, 2010.
- 677 Ashley, W. S. and Mote, T. L.: Derecho hazards in the United States, *Bulletin of the American Meteorological*  
678 *Society*, 86, 1577-1592, <https://doi.org/10.1175/BAMS-86-11-1577>, 2005.
- 679 Bardis, M., Houshyar, R., Chantaduly, C., Ushinsky, A., Glavis-Bloom, J., Shaver, M., Chow, D., Uchio, E.,  
680 and Chang, P.: Deep learning with limited data: Organ segmentation performance by U-Net, *Electronics*, 9,  
681 1199, <https://doi.org/10.3390/electronics9081199>, 2020.
- 682 Bentley, M. L. and Mote, T. L.: A climatology of derecho-producing mesoscale convective systems in the  
683 central and eastern United States, 1986–95. Part I: Temporal and spatial distribution, *Bulletin of the American*  
684 *Meteorological Society*, 79, 2527-2540, [https://doi.org/10.1175/1520-0477\(1998\)079<2527:ACODPM>2.0.CO;2](https://doi.org/10.1175/1520-0477(1998)079<2527:ACODPM>2.0.CO;2), 1998.
- 686 Bentley, M. L. and Sparks, J. A.: A 15 yr climatology of derecho-producing mesoscale convective systems over  
687 the central and eastern United States, *Climate research*, 24, 129-139, <https://www.jstor.org/stable/24868368>,  
688 2003.
- 689 Bowman, K. P. and Homeyer, C. R.: GridRad - Three-Dimensional Gridded NEXRAD WSR-88D Radar Data,  
690 the National Center for Atmospheric Research, Computational and Information Systems Laboratory [dataset],  
691 <https://doi.org/10.5065/D6NK3CR7>, 2017 (last access: 3 November 2022).
- 692 CDIACS/EOL/NCAR/UCAR and CPC/NCEP/NWS/NOAA: NCEP/CPC Four Kilometer Precipitation Set,  
693 Gauge and Radar, the National Center for Atmospheric Research, Computational and Information Systems  
694 Laboratory [dataset], <https://doi.org/10.5065/D69Z93M3>, 2000 (last access: 31 October 2022).
- 695 Coniglio, M. C. and Stensrud, D. J.: Interpreting the climatology of derechos, *Weather and forecasting*, 19,  
696 595-605, [https://doi.org/10.1175/1520-0434\(2004\)019<0595:ITCOD>2.0.CO;2](https://doi.org/10.1175/1520-0434(2004)019<0595:ITCOD>2.0.CO;2), 2004.
- 697 Corfidi, S. F., Coniglio, M. C., Cohen, A. E., and Mead, C. M.: A proposed revision to the definition of  
698 “derecho”, *Bulletin of the American Meteorological Society*, 97, 935-949, <https://doi.org/10.1175/BAMS-D-14-00254.1>, 2016.
- 700 Evans, J. S. and Doswell, C. A.: Examination of derecho environments using proximity soundings, *Weather*  
701 *and Forecasting*, 16, 329-342, [https://doi.org/10.1175/1520-0434\(2001\)016<0329:EODEUP>2.0.CO;2](https://doi.org/10.1175/1520-0434(2001)016<0329:EODEUP>2.0.CO;2), 2001.
- 702 Feng, Z., Hardin, J., Barnes, H. C., Li, J., Leung, L. R., Varble, A., and Zhang, Z.: PyFLEXTRKR: a flexible  
703 feature tracking Python software for convective cloud analysis, *Geoscientific Model Development*, 16, 2753-  
704 2776, <https://doi.org/10.5194/gmd-16-2753-2023>, 2023.
- 705 Feng, Z., Houze, R. A., Leung, L. R., Song, F., Hardin, J. C., Wang, J., Gustafson, W. I., and Homeyer, C. R.:  
706 Spatiotemporal characteristics and large-scale environments of mesoscale convective systems east of the  
707 Rocky Mountains, *Journal of Climate*, 32, 7303-7328, <https://doi.org/10.1175/JCLI-D-19-0137.1>, 2019.
- 708 Feng, Z., Leung, L. R., Liu, N., Wang, J., Houze Jr, R. A., Li, J., Hardin, J. C., Chen, D., and Guo, J.: A global  
709 high-resolution mesoscale convective system database using satellite-derived cloud tops, surface precipitation,



- 710 and tracking, *Journal of Geophysical Research: Atmospheres*, 126, e2020JD034202,  
711 <https://doi.org/10.1029/2020JD034202>, 2021.
- 712 Fujita, T. T.: Proposed characterization of tornadoes and hurricanes by area and intensity, 1971.
- 713 Galea, D., Ma, H.-Y., Wu, W.-Y., and Kobayashi, D.: Deep Learning Image Segmentation for Atmospheric  
714 Rivers, *Artificial Intelligence for the Earth Systems*, 3, 230048, <https://doi.org/10.1175/AIES-D-23-0048.1>,  
715 2024.
- 716 Geiss, A. and Hardin, J. C.: Radar super resolution using a deep convolutional neural network, *Journal of*  
717 *Atmospheric and Oceanic Technology*, 37, 2197-2207, <https://doi.org/10.1175/JTECH-D-20-0074.1>, 2020.
- 718 Geiss, A., Li, J., Feng, Z., and Leung, L. R.: Bow echo detection and segmentation, Zenodo [dataset],  
719 <https://doi.org/10.5281/zenodo.10822721>, 2024 (last access: 15 March 2024).
- 720 Guastini, C. T. and Bosart, L. F.: Analysis of a progressive derecho climatology and associated formation  
721 environments, *Monthly Weather Review*, 144, 1363-1382, <https://doi.org/10.1175/MWR-D-15-0256.1>, 2016.
- 722 Hersbach, H., Bell, B., Berrisford, P., Biavati, G., Horányi, A., Muñoz Sabater, J., Nicolas, J., Peubey, C.,  
723 Radu, R., Rozum, I., Schepers, D., Simmons, A., Soci, C., Dee, D., and Thépaut, J.-N.: ERA5 hourly data on  
724 single levels from 1940 to present, Copernicus Climate Change Service (C3S) Climate Data Store (CDS)  
725 [dataset], <https://doi.org/10.24381/cds.adbb2d47>, 2023 (last access: 1 November 2022).
- 726 Huang, G., Liu, Z., Pleiss, G., Van Der Maaten, L., and Weinberger, K. Q.: Convolutional networks with dense  
727 connectivity, *IEEE transactions on pattern analysis and machine intelligence*, 44, 8704-8716,  
728 <https://doi.org/10.1109/TPAMI.2019.2918284>, 2019.
- 729 Huang, H., Lin, L., Tong, R., Hu, H., Zhang, Q., Iwamoto, Y., Han, X., Chen, Y.-W., and Wu, J.: Unet 3+: A  
730 full-scale connected unet for medical image segmentation, ICASSP 2020-2020 IEEE international conference  
731 on acoustics, speech and signal processing (ICASSP), 1055-1059,  
732 <https://doi.org/10.1109/ICASSP40776.2020.9053405>,
- 733 Janowiak, J., Joyce, B., and Xie, P.: NCEP/CPC L3 Half Hourly 4km Global (60S - 60N) Merged IR V1,  
734 Goddard Earth Sciences Data and Information Services Center (GES DISC) [dataset],  
735 <https://doi.org/10.5067/P4HZB9N27EKU>, 2017 (last access: 27 September 2022).
- 736 Johns, R. H. and Hirt, W. D.: Derechos: Widespread convectively induced windstorms, *Weather and*  
737 *Forecasting*, 2, 32-49, [https://doi.org/10.1175/1520-0434\(1987\)002<0032:DWCIW>2.0.CO;2](https://doi.org/10.1175/1520-0434(1987)002<0032:DWCIW>2.0.CO;2), 1987.
- 738 Ketkar, N.: Introduction to keras, *Deep learning with python: a hands-on introduction*, 97-111,  
739 [https://doi.org/10.1007/978-1-4842-2766-4\\_7](https://doi.org/10.1007/978-1-4842-2766-4_7), 2017.
- 740 Kingma, D. P. and Ba, J.: Adam: A method for stochastic optimization, arXiv preprint arXiv:1412.6980,  
741 <https://doi.org/10.48550/arXiv.1412.6980>, 2014.
- 742 Knapp, K. R., Diamond, H. J., Kossin, J. P., Kruk, M. C., and Schreck, C. J. I.: International Best Track  
743 Archive for Climate Stewardship (IBTrACS) Project, Version 4, [North Atlantic], NOAA National Centers for  
744 Environmental Information [dataset], <https://doi.org/10.25921/82ty-9e16>, 2018 (last access: 5 March 2024).



- 745 Knapp, K. R., Kruk, M. C., Levinson, D. H., Diamond, H. J., and Neumann, C. J.: The international best track  
746 archive for climate stewardship (IBTrACS) unifying tropical cyclone data, *Bulletin of the American*  
747 *Meteorological Society*, 91, 363-376, <https://doi.org/10.1175/2009BAMS2755.1>, 2010.
- 748 Kumler-Bonfanti, C., Stewart, J., Hall, D., and Govett, M.: Tropical and extratropical cyclone detection using  
749 deep learning, *Journal of Applied Meteorology and Climatology*, 59, 1971-1985,  
750 <https://doi.org/10.1175/JAMC-D-20-0117.1>, 2020.
- 751 Lagerquist, R., Turner, D., Ebert-Uphoff, I., Stewart, J., and Hagerty, V.: Using deep learning to emulate and  
752 accelerate a radiative transfer model, *Journal of Atmospheric and Oceanic Technology*, 38, 1673-1696,  
753 <https://doi.org/10.1175/JTECH-D-21-0007.1>, 2021.
- 754 Li, J., Feng, Z., Qian, Y., and Leung, L. R.: A high-resolution unified observational data product of mesoscale  
755 convective systems and isolated deep convection in the United States for 2004–2017, *Earth Syst. Sci. Data*, 13,  
756 827-856, <https://doi.org/10.5194/essd-13-827-2021>, 2021.
- 757 Li, J., Geiss, A., Feng, Z., and Leung, L. R.: A derecho climatology over the United States from 2004 to 2021,  
758 Zenodo [dataset], <https://doi.org/10.5281/zenodo.10884046>, 2024 (last access: 27 March 2024).
- 759 Mounier, A., Raynaud, L., Rottner, L., Plu, M., Arbogast, P., Kreitz, M., Mignan, L., and Touzé, B.: Detection  
760 of bow echoes in kilometer-scale forecasts using a convolutional neural network, *Artificial Intelligence for the*  
761 *Earth Systems*, 1, e210010, <https://doi.org/10.1175/AIES-D-21-0010.1>, 2022.
- 762 NOAA/NCEI: Global Hourly - Integrated Surface Database (ISD), the National Oceanic and Atmospheric  
763 Administration (NOAA) National Centers for Environmental Information (NCEI) [dataset],  
764 <https://www.ncei.noaa.gov/data/global-hourly/archive/isd/>, 2001 (last access: 21 January 2023).
- 765 NOAA/NCEI: Federal Climate Complex Data Documentation For Integrated Surface Data (ISD), 126,  
766 <https://www.ncei.noaa.gov/data/global-hourly/doc/isd-format-document.pdf>, 2018.
- 767 Ouali, Y., Hudelot, C., and Tami, M.: An overview of deep semi-supervised learning, arXiv preprint  
768 arXiv:2006.05278, <https://doi.org/10.48550/arXiv.2006.05278>, 2020.
- 769 Peláez-Vegas, A., Mesejo, P., and Luengo, J.: A Survey on Semi-Supervised Semantic Segmentation, arXiv  
770 preprint arXiv:2302.09899, <https://doi.org/10.48550/arXiv.2302.09899>, 2023.
- 771 Ronneberger, O., Fischer, P., and Brox, T.: U-net: Convolutional networks for biomedical image segmentation,  
772 *Medical Image Computing and Computer-Assisted Intervention–MICCAI 2015: 18th International*  
773 *Conference, Munich, Germany, October 5-9, 2015, Proceedings, Part III* 18, 234-241,  
774 [https://doi.org/10.1007/978-3-319-24574-4\\_28](https://doi.org/10.1007/978-3-319-24574-4_28),
- 775 Sha, Y., Gagne II, D. J., West, G., and Stull, R.: Deep-learning-based gridded downscaling of surface  
776 meteorological variables in complex terrain. Part I: Daily maximum and minimum 2-m temperature, *Journal of*  
777 *Applied Meteorology and Climatology*, 59, 2057-2073, <https://doi.org/10.1175/JAMC-D-20-0057.1>, 2020.
- 778 Smith, A., Lott, N., and Vose, R.: The integrated surface database: Recent developments and partnerships,  
779 *Bulletin of the American Meteorological Society*, 92, 704-708, <https://doi.org/10.1175/2011BAMS3015.1>,  
780 2011.



- 781 Squitieri, B. J., Wade, A. R., and Jirak, I. L.: A historical overview on the science of derechos: part I:  
782 identification, climatology, and societal impacts, *Bulletin of the American Meteorological Society*, 104, E1709-  
783 E1733, <https://doi.org/10.1175/BAMS-D-22-0217.1>, 2023.
- 784 Starzec, M., Homeyer, C. R., and Mullendore, G. L.: Storm labeling in three dimensions (SL3D): A volumetric  
785 radar echo and dual-polarization updraft classification algorithm, *Monthly Weather Review*, 145, 1127-1145,  
786 <https://doi.org/10.1175/MWR-D-16-0089.1>, 2017.
- 787 Taha, A. A. and Hanbury, A.: Metrics for evaluating 3D medical image segmentation: analysis, selection, and  
788 tool, *BMC medical imaging*, 15, 1-28, <https://doi.org/10.1186/s12880-015-0068-x>, 2015.
- 789 Van Engelen, J. E. and Hoos, H. H.: A survey on semi-supervised learning, *Machine learning*, 109, 373-440,  
790 <https://doi.org/10.1007/s10994-019-05855-6>, 2020.
- 791 Weisman, M. L.: The genesis of severe, long-lived bow echoes, *Journal of the atmospheric sciences*, 50, 645-  
792 670, [https://doi.org/10.1175/1520-0469\(1993\)050<0645:TGOSLL>2.0.CO;2](https://doi.org/10.1175/1520-0469(1993)050<0645:TGOSLL>2.0.CO;2), 1993.
- 793 Weyn, J. A., Durran, D. R., Caruana, R., and Cresswell-Clay, N.: Sub-seasonal forecasting with a large  
794 ensemble of deep-learning weather prediction models, *Journal of Advances in Modeling Earth Systems*, 13,  
795 e2021MS002502, <https://doi.org/10.1029/2021MS002502>, 2021.
- 796 White, C. H., Ebert-Uphoff, I., Haynes, J. M., and Noh, Y.-J.: Super-Resolution of GOES-16 ABI Bands to a  
797 Common High Resolution with a Convolutional Neural Network, *Artificial Intelligence for the Earth Systems*,  
798 <https://doi.org/10.1175/AIES-D-23-0065.1>, 2024.
- 799 Whitehall, K., Mattmann, C. A., Jenkins, G., Rwebangira, M., Demoz, B., Waliser, D., Kim, J., Goodale, C.,  
800 Hart, A., and Ramirez, P.: Exploring a graph theory based algorithm for automated identification and  
801 characterization of large mesoscale convective systems in satellite datasets, *Earth Science Informatics*, 8, 663-  
802 675, <https://doi.org/10.1007/s12145-014-0181-3>, 2015.
- 803